Triatomic butterfly molecules

Matthew T Eiles[1] , **Christian Fey**[2], **Frederic Hummel**[3] **and Peter Schmelcher**[3,4]

[1] Max-Planck-Institut für Physik komplexer Systeme, Nöthnitzer Str. 38, D-01187 Dresden, Germany
[2] Max-Planck-Institute of Quantum Optics, Hans-Kopfermann-Strasse. 1, D-85748 Garching, Germany
[3] Zentrum für Optische Quantentechnologien, Fachbereich Physik, Universität Hamburg, Luruper Chaussee 149, D-22761 Hamburg, Germany
[4] The Hamburg Centre for Ultrafast Imaging, Universität Hamburg, Luruper Chaussee 149, D-22761 Hamburg, Germany

E-mail: meiles@mpg.pks.de

Abstract

We detail the rich electronic and vibrational structure of triatomic 'butterfly' molecules, ultra-long-range Rydberg molecules bound by resonant p-wave scattering. We divide these molecules into two sub-classes depending on their parity under reflection of the electronic wave function through the molecular plane. The trimers with odd reflection parity have smoothly varying, non-oscillatory potential energy surfaces except near the collinear configuration. Here, the vibrational wave function is confined tightly in the symmetric-stretch and bending modes, but only loosely in the asymmetric stretch mode. The trimers with even reflection parity exhibit far richer potential surfaces with abundant minima, but only a few of these are deep enough to localize the vibrational states. These minima are correlated with the electronic wave functions of the butterfly dimer, contributing to a building principle for trimers.

Keywords: external fields, ultralong-range molecules, rydberg states

(Some figures may appear in colour only in the online journal)

1. Introduction

With very few exceptions, atomic negative ions—weakly bound systems composed of an electron (e^-) and a neutral atom (B)—possess only a single bound state [1, 2]. In the alkali atoms this is the ^1S state, bound by about 500 meV. For several years the existence of an excited ^3P state in cesium was under debate until photodetachment experiments eventually revealed that it is in fact an unbound shape resonance [3–9]. Indeed, all alkali species possess a p-wave shape resonance just a few meV above threshold [1, 2, 10].

Despite the transient nature of these resonances, they are responsible for the formation of a class of ultra-long-range Rydberg molecules known as 'butterflies.' A butterfly molecule consists of a Rydberg atom ($B^+ + e^-$) bound to a neutral ground state atom (B) via the $e^- + B$ p-wave scattering interaction, which leads at resonance to a short-lived ion-pair state [11–13]. Superimposed onto this ion-pair potential is the oscillatory structure of the Rydberg wave function, and vibrational states form in the resulting potential wells. Butterfly molecules have been observed in rubidium and, due to

their large dipole moments, exhibit pendulum behavior in weak external fields [14, 15].

In this article, we show that this p-wave binding mechanism can bind a second ground-state atom to the Rydberg atom, forming a triatomic butterfly molecule. Other ultra-long-range triatomic Rydberg molecules formed by the s-wave scattering interaction have been studied previously theoretically and experimentally [16–23], but a study of the butterfly trimer's full electronic and vibrational structure has not yet been attempted. We determine this structure by computing, analyzing, and interpreting the underlying three-dimensional potential energy surfaces based on the Born–Oppenheimer approximation and the resulting nuclear eigenstates. The latter are obtained using a combined discrete variable and finite difference approach. This effort is simplified by the fact that the potential surfaces decouple into two groups distinguished by their electronic parity under reflection through the molecular plane. We refer to these two classes as *odd* and *even* butterfly trimers. The equilibrium geometries supporting trimer states vary greatly between these two classes: the odd butterflies have only a few minima
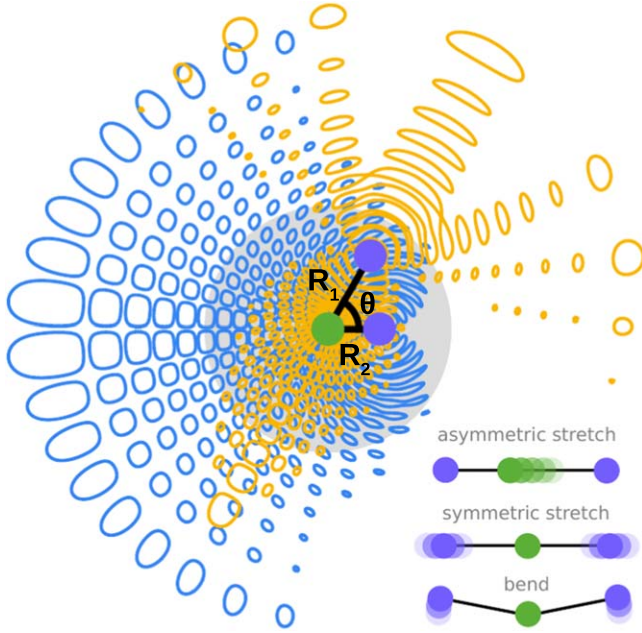
Figure 1. A schematic of the $n = 30$ butterfly trimer. The two ground-state atoms are marked in purple, and the Rydberg atom is shown in green. The approximate range of bond lengths considered in this butterfly regime lie within the shaded region. The electronic densities of the θ_2-butterfly and the R_1-butterfly are depicted in blue and yellow contours, respectively, where each contour specifies when the wave function amplitude evaluated in the molecular plane equals $1 \times 10^{-4.8}$. The two bond lengths and bending angle are labeled. On the lower right the three types of nuclear motion exhibited by the trimer are depicted.

in a constrained range of possible molecular geometries close to the collinear arrangement, whereas the even butterflies possess a plethora of equilibrium configurations with a rich diversity in the electronic character. The geometries at which these minima occur can be analyzed and understood from features in the electronic wave functions of the diatomic butterfly molecule.

In section 2 we discuss our approach to the electronic structure of the trimers and, specifically, their Born–Oppenheimer adiabatic potential energy surfaces. Sections 3 and 4 are dedicated to a discussion of the equilibrium configurations and geometries and the development of a building principles for the even trimers, respectively. Section 5 analyzes the vibrational dynamics of our butterfly trimers. Finally, section 6 contains our brief conclusions and an outlook.

2. Computational approach to the electronic structure and Born–Oppenheimer potential energy surfaces

The eigenenergies of the electronic Hamiltonian for fixed nuclei represent the Born–Oppenheimer potential energy surfaces. For our trimers, they depend on the two bond lengths, R_1 and R_2, and a single bending angle, θ. This geometry is illustrated in figure 1. The trimer can exhibit three vibrational modes: a symmetric stretch, in which $R_1 = R_2$; an

asymmetric stretch, in which R_1 grows while R_2 shrinks (or vice versa); and a bending mode in which θ oscillates.

The interaction of the electron with a ground-state atom is given by the Fermi pseudopotential, generalized by Omont to arbitrary partial waves [24, 25]. Including contributions from s- and p-scattering partial waves only, we obtain the Hamiltonian

$$H(\vec{r}; R_1, R_2, \theta) = -\sum_{nlm} \frac{|nlm\rangle \langle nlm|}{2(n - \mu_l)^2} + 2\pi \sum_{i=1}^{2} \sum_{\xi=1}^{4} a_i^{(\xi)} |i\xi\rangle \langle i\xi|. \quad (1)$$

The first line describes the Rydberg atom using its known eigenfunctions $\phi_{nlm}(\vec{r}) = \frac{u_{nl}(r)}{r} Y_{lm}(\theta, \varphi) = \langle \vec{r}|nlm\rangle$ and eigenenergies $-\frac{1}{2(n - \mu_l)^2}$, where n is the principal quantum number and l and m are the orbital and magnetic quantum numbers. For a given n only a few states with $l \leqslant l_{\min}$ have non-vanishing quantum defects μ_l which shift them out of the degenerate manifold of high-l states. The second line of equation (1) describes the electron–atom interactions using the Fermi–Omont pseudopotential operator, $\hat{V}^{(i\xi)} = |i\xi\rangle \langle i\xi|$, which has the following matrix representation in the Rydberg basis

$$\hat{V}^{(i\xi)}_{n'l'm',nlm} = \tilde{\partial}_\xi [\phi_{n'l'm'}(\vec{r})]^* \tilde{\partial}_\xi [\phi_{nlm}(\vec{r})] |_{\vec{r}=\vec{R}_i}. \quad (2)$$

This employs a shorthand for the derivative operators used in the pseudopotentials: $\tilde{\partial}_{\xi=1} = 1$, $\tilde{\partial}_{\xi=2} = \partial_r$, $\tilde{\partial}_{\xi=3} = \frac{1}{r}\partial_\theta$, and $\tilde{\partial}_{\xi=4} = \frac{1}{r\sin\theta}\partial_\varphi$. The three $\xi > 1$ terms correspond to the three components of the gradient in the p-wave operator. The scattering volumes are $a_i^{(\xi=1)} = a_s[k(R_i)]$ and $a_i^{(\xi>1)} = 3a_p^3[k(R_i)]$. Equation (1) neglects all spin degrees of freedom, and assumes the scattering occurs only in the triplet channel [26–29].

A convenient approach to diagonalize equation (1) has been developed which does not require the complete Rydberg basis. For a given i, ξ, n, and for $l > l_{\min}$, the matrix defined in equation (2) has a single non-trivial eigenstate. It follows that there are four 'dimer orbitals' in total for each atom, $i = 1, 2$: one 'trilobite' for $\xi = 1$, an 'R_i-butterfly' for $\xi = 2$, a 'θ_i-butterfly' for $\xi = 3$, and a 'φ_i-butterfly' for $\xi = 4$. Figure 1 shows two of these dimer orbitals, the R_1-butterfly (orange) and θ_2-butterfly (blue). The nodal structures of the butterfly dimer orbitals are arranged such that, at the position of the ground state atom, the wave function changes most rapidly parallel to (R-butterfly) or perpendicular to (θ- and φ-butterflies, in mutually orthogonal directions) the internuclear axis. The R-butterfly orbital therefore concentrates electron probability around the internuclear axis, while in the θ- and φ-butterflies the electronic density fans out over a larger area. The electronic energies of the θ-butterfly and φ-butterfly dimer orbitals are degenerate. In general, the dimer orbitals are not orthogonal: a $\xi = \alpha$ orbital for the atom located at $\vec{R}_p$ has an overlap with the $\xi = \beta$ orbital at position $\vec{R}_q$ equal to [16, 17, 19, 23]

$$\Upsilon_{pq}^{\alpha\beta} = \sum_{l > l_{\min}}^{n-1} \sum_{m=-l}^{m=l} \tilde{\partial}_\alpha [\phi_{nlm}(\vec{R}_p)]^* \tilde{\partial}_\beta \phi_{nlm}(\vec{R}_q). \quad (3)$$

Several of these overlap elements vanish at specific geometries. As detailed in [19, 30], the projection of the orbital angular momentum of the $\xi = 2$ orbital onto the internuclear axis is zero, while it is unity for the $\xi = 3$ and $\xi = 4$ orbitals. Therefore, the matrix elements Υ_{ii}^{23} and Υ_{ii}^{24} vanish. Furthermore, the $\xi = 4$ orbital has odd parity under reflection through the molecular plane, i.e. $\varphi \to -\varphi$, while the $\xi = 2$ orbital is independent of this angle and the $\xi = 3$ orbital is an even function of φ. Thus, both $\xi = 2, 3$ orbitals have even parity under this same operation. This implies that these orbitals decouple completely from $\xi = 4$, i.e. $\Upsilon_{ii'}^{4\beta} = 0$ for $\beta = 2, 3$. For this reason, in this paper we distinguish between the *even* trimers, which are linear combinations of the R_1, R_2, θ_1, and θ_2 dimer orbitals, and the *odd* trimers, linear combinations of the two φ_1 and φ_2 dimer orbitals.

Due to the effects of the *p*-wave resonance, the trilobite states are energetically decoupled from the butterfly states and from other *n* manifolds, and to a good approximation can be studied independently. References [17, 23] have already investigated the trilobite trimer, i.e. the states defined by the Hamiltonian in the 2×2 trilobite subspace:

$$\widetilde{H}_t = \begin{pmatrix} a_1^{(1)}[k(R_1)]\Upsilon_{11}^{11} & a_1^{(1)}[k(R_1)]\Upsilon_{12}^{11} \\ a_1^{(1)}[k(R_2)]\Upsilon_{21}^{11} & a_1^{(1)}[k(R_2)]\Upsilon_{22}^{11} \end{pmatrix}, \quad (4)$$

where the overall Rydberg energy $-\frac{1}{2n^2}$ has been set to zero. This separation of trilobite and butterfly states implies that the butterfly states of a single *n* manifold are governed by the Hamiltonian $\widetilde{H}_b$:

$$\begin{pmatrix} a_1^{(2)}\Upsilon_{11}^{22} & a_1^{(2)}\Upsilon_{21}^{22} & 0 & a_1^{(2)}\Upsilon_{21}^{32} & 0 & 0 \\ a_2^{(2)}\Upsilon_{12}^{22} & a_2^{(2)}\Upsilon_{22}^{22} & a_2^{(2)}\Upsilon_{12}^{32} & 0 & 0 & 0 \\ 0 & a_1^{(3)}\Upsilon_{21}^{23} & a_1^{(3)}\Upsilon_{11}^{33} & a_1^{(3)}\Upsilon_{21}^{33} & 0 & 0 \\ a_2^{(3)}\Upsilon_{12}^{23} & 0 & a_2^{(3)}\Upsilon_{12}^{33} & a_2^{(3)}\Upsilon_{22}^{33} & 0 & 0 \\ 0 & 0 & 0 & 0 & a_1^{(4)}\Upsilon_{11}^{44} & a_1^{(4)}\Upsilon_{21}^{44} \\ 0 & 0 & 0 & 0 & a_2^{(4)}\Upsilon_{12}^{44} & a_2^{(4)}\Upsilon_{22}^{44} \end{pmatrix}. \quad (5)$$

Note that in equations (4) and (5) the Hamiltonian marked by a tilde is modified from the original Hamiltonian H since it includes the effect of the non-orthogonal basis:

$$\underbrace{\Upsilon^{-1}H}_{\widetilde{H}}\psi = E\underbrace{\Upsilon^{-1}\Upsilon}_{1}\psi. \quad (6)$$

The studies of trilobite trimers in [16, 23] found that the eigenvalues of equation (4) are nearly identical to those computed using the full Rydberg basis, consisting of states with finite quantum defects and multiple Rydberg manifolds. This is because the coupling between the trilobite and these other states is negligible. However, this same treatment fails catastrophically for studies of butterfly states as it is impossible to obtain even qualitatively accurate predictions within perturbation theory. The *p*-wave shape resonance causes the scattering volume to diverge, and the butterfly potential surfaces are only constrained to finite values via coupling to additional Rydberg manifolds. Additionally, the butterfly potential surface plunges through and couples to all quantum

defect states before being repelled from the lower Rydberg manifold [11]. This coupling is quantitatively important.

These problems are addressed by including trilobite and butterfly dimer orbitals for several *n* manifolds ($\mathcal{M}$ is the number of manifolds) as well as the atomic basis states which have non-zero quantum defects in a hybrid basis [19, 30]. The potential energy surfaces obtained with this method are identical to those computed via the full diagonalization using the Rydberg basis implied in equation (1), but have the advantage of a much more compact matrix representation. The Hamiltonian for a *N*-perturber molecule in this basis is written

$$\widetilde{H} = \begin{pmatrix} O_{PP'} & 0 \\ 0 & 1_{QQ'} \end{pmatrix}^{-1} \begin{pmatrix} H_{PP'} & H_{PQ'} \\ H_{QP'} & H_{QQ'} \end{pmatrix}, \quad (7)$$

where the sub-block $H_{PP'}$ of dimension $4\mathcal{M}N$, the quantum defect sub-block $H_{QQ'}$ of dimension $\mathcal{M}(l_{\min} + 1)^2$, and the overlap matrix $O_{PP'}$ have matrix elements

$$H_{PP'} = -\frac{1}{2n^2}\Upsilon_{pq,n}^{\alpha\beta}\delta_{nn'}$$
$$+ 2\pi\sum_{i=1}^{N}\sum_{\xi=1}^{4}a_i^{(\xi)}\Upsilon_{pi,n}^{\alpha\xi}\Upsilon_{iq,n'}^{\xi\beta}, \quad (8)$$

$$H_{QQ'} = -\frac{\delta_{nn'}\delta_{ll'}}{2(n-\mu_l)^2}$$
$$+ 2\pi\sum_{i=1}^{N}\sum_{\xi=1}^{4}a_i^{(\xi)}\phi_{nlm}^{\xi}(R_i)^*\phi_{n'l'm'}^{\xi}(R_i) \quad (9)$$

$$O_{PP'} = \Upsilon_{pq,n}^{\alpha\beta}\delta_{nn'}. \quad (10)$$

Additionally, there are coupling terms between dimer orbitals and the low $-l$ quantum defect states

$$H_{PQ'} = 2\pi\sum_{i=1}^{N}\sum_{\xi=1}^{4}a_i^{(\xi)}\Upsilon_{pi,n}^{\alpha\xi}\phi_{n'l'm'}^{\xi}(R_i). \quad (11)$$

In our present calculations we use the $n = 29,30$, and 31 Rydberg manifolds and include quantum defects for *s*, *p*, and *d* waves ($l_{\min} = 2$). These parameters give adequately converged potential energy surfaces for reasonable qualitative results. Using a zero-range pseudopotential entails the assumption of several approximations which can become poor at small internuclear distances. However, recent experiments in this regime[14, 31] along with comparisons with more accurate theoretical approaches [11, 13, 32] have shown that, for $R > 100a_0$, the pseudopotential remains quite accurate, especially considering our neglect of spin-dependent interactions which is a much larger source of error. We emphasize that our goal is to provide quantitatively accurate results within our stated approximations and use these to build up a qualitatively rigorous analysis of the structure of these molecules.

3. Analysis of adiabatic potential energy surfaces

For the paradigmatic Rydberg state studied here, $n = 30$, the allowed range of internuclear distances for the butterfly states is $R_i \in (100, 600)$. This range is determined by the energy dependence of the *p*-wave scattering volume, which in turn depends on *R* through the semiclassical kinetic energy of the electron, $k(R)^2 = 2R^{-1} - n^{-2}$. The bond length R_{res} associated with the shape resonance is therefore determined by the
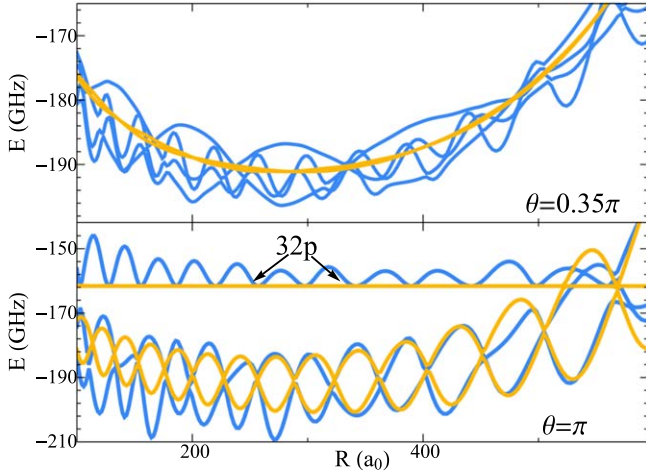
Figure 2. Breathing mode slices of the Rb_3 potential surface for different bending angles θ. Note the different energy axes in the two panels. The orange and blue curves have odd and even parity, respectively. The energies are relative to the hydrogenic $n = 30$ energy. The potential energy surface associated with the $32p$ state cuts through the lower panel.

equation $2R_{res}^{-1} - n^{-2} = 2E_{res}$. For $n = 30$, $R_{res} \approx 600 \, a_0$. It varies slowly as a function of n. The typical bond lengths of these molecules therefore do not scale proportional to n^2 as in the trilobite molecules. Just as E_{res} varies among atomic species, so do these typical bond lengths [10].

The three-dimensional potential surfaces are challenging to visually investigate. Therefore, to get an impression of their behavior, we first exhibit in figure 2 the breathing mode potential curves (symmetric stretch vibration): these are cuts through the surface with varying $R = R_1 = R_2$ and fixed θ. The two odd trimer potential curves (orange) oscillate dramatically in the collinear configuration, but at $\theta = 0.35\pi$ they are very smooth and almost degenerate with each other and with the diatomic potential energy curve for the $\xi = 4$ state (see figure 6). The four even trimer curves, on the other hand, oscillate for all values of θ. When $\theta = \pi$, two of the potential curves become degenerate with the odd-trimer curves. For $\theta \neq \pi$, the even trimer curves separate into two sets having relatively fast and slow oscillation frequencies, respectively. The quickly (slowly) varying curves are predominantly mixtures of R_1 and R_2 (θ_1 and θ_2) dimer orbitals, as the coupling Υ_{12}^{23} is typically small.

To gain further insight, we must move beyond the impediment of these low-dimensional potential cuts. Figure 3 presents the energetically deepest potential energy surface of the odd trimer state as a contour plot in the three nuclear coordinates. The deepest energy contours are only found near the collinear geometry ($\theta = \pi$), where cylindrically shaped wells around deep minima can be found. As θ decreases from π, the potential surface quickly becomes independent of θ, and hence the constant energy contours become quite flat. Figure 4 shows the full potential energy surface $V(R_1, R_2, \theta)$ for the same two fixed angles $\theta = \pi, 0.35\pi$ as in figure 2. This shows in more detail the deep potential wells in the
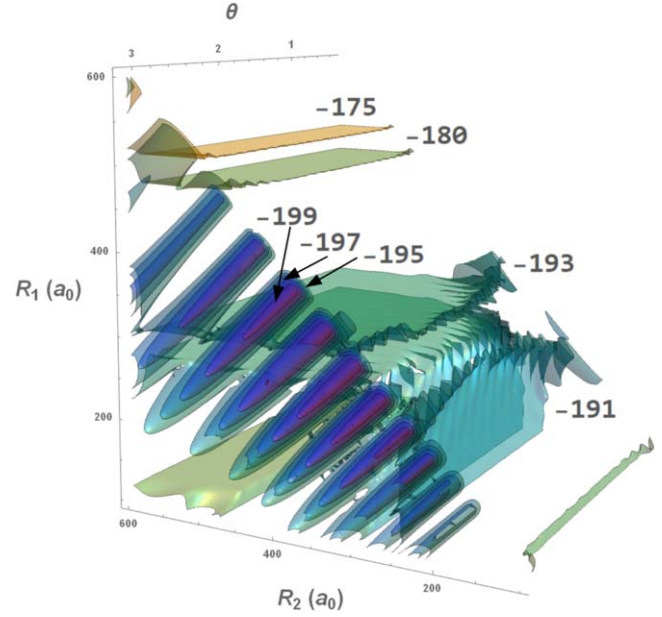

Figure 3. Contours of the complete potential energy surface for the odd trimer state. Each contour, specified by a different color, represents a surface of constant energy whose value is given in GHz in each label. The deepest contours are only found near the $\theta = \pi$ plane, and the higher energy contours are insensitive to changes in θ. Since the potentials are symmetric with respect to reflection across the $R_1 = R_2$ line, the contours are not shown for $R_1 > R_2$ for clarity.

collinear geometry and the nearly featureless surfaces at other arrangements.

These properties of the potential surfaces can be understood by analyzing the qualitative structure of the Hamiltonian more closely, focusing on the $\xi = 4$ sub-block of equation (5). In this subspace the two odd trimer potential surfaces are

$$\varepsilon_{\pm}(\vec{R}_1, \vec{R}_2) = \frac{\varepsilon_d(R_1) + \varepsilon_d(R_2)}{2}$$
$$\pm \frac{1}{2}\sqrt{[\varepsilon_d(R_1) - \varepsilon_d(R_2)]^2 + 4c(\vec{R}_1, \vec{R}_2)}, \quad (12)$$

where the cross term is

$$c(\vec{R}_1, \vec{R}_2) = 4a_1^{(4)}a_2^{(4)} \left| \sum_{l > l_{min}}^{n-1} D_{l1}(R_1, 0)D_{l1}(R_2, \theta) \right|^2 ;$$
$$D_{lm}(R, \theta) = m \frac{u_{nl}(R)}{R^2} \frac{Y_{lm}(\theta, 0)}{\sin\theta}, \quad (13)$$

and the dimer potential is

$$\varepsilon_d(R) = a_1^{(4)} \sum_{l > l_{min}}^{n-1} \left| \frac{u_{nl}(R)}{R^2} \right|^2 \frac{(2l+1)(l+1)l}{8\pi}. \quad (14)$$

When $c(\vec{R}_1, \vec{R}_2)$ vanishes, the trimer potentials reduce to independent dimer potentials, $\varepsilon_+(\vec{R}_1, \vec{R}_2) = \max[\varepsilon_d(R_1), \varepsilon_d(R_2)]$, $\varepsilon_-(\vec{R}_1, \vec{R}_2) = \min[\varepsilon_d(R_1), \varepsilon_d(R_2)]$, which are smooth and have a single global minimum. The cross-term induces mixing and creates additional wells in the potentials; however, it depends very sharply on θ, $c(\vec{R}_1, \vec{R}_2) \sim \frac{1}{\sin^4\theta}$. This explains the appearance of interesting triatomic features only near the collinear geometry where $\theta = \pi$. We exclude angles near $\theta = 0$
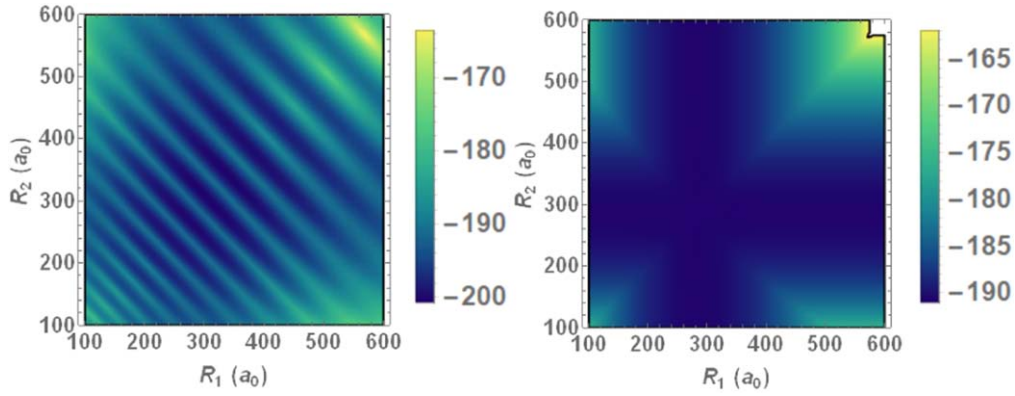
Figure 4. Odd parity potential surfaces at $\theta = \pi$ and $\theta = 0.35\pi$ (left and right, respectively). The units of potential energy are in GHz.
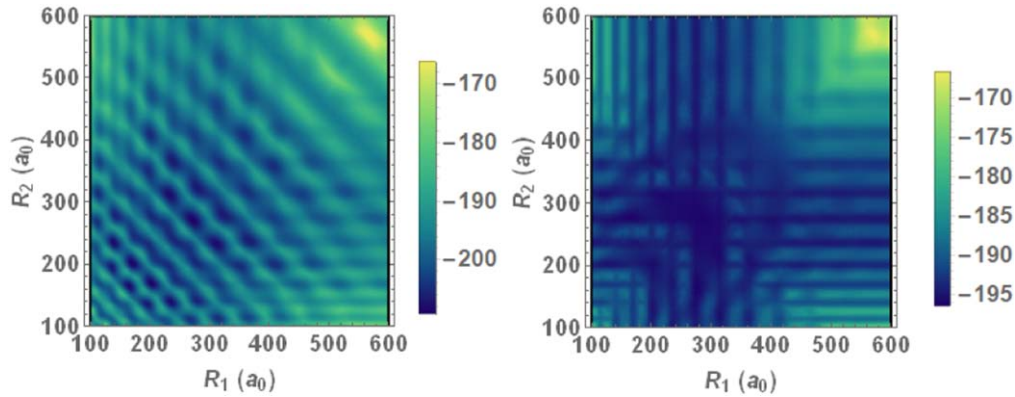

Figure 5. Even trimer potential surfaces at $\theta = \pi$ and $\theta = 0.35\pi$ (left and right, respectively). The units of potential energy are in GHz.

from our analysis as we have not included atom-atom interactions which would become highly relevant at these geometries.

In contrast to the simplicity of the odd trimer potential surfaces, the even trimer potential surfaces are highly complex, varying much more rapidly as a function of all coordinates, but particularly as a function of θ. For this reason a contour plot visualization is unintelligible, and we only show radial potential cuts in figure 5 at the same two angles as before. These have minima at a plethora of stable molecular geometries. By comparing the two panels in figure 5 we find that the potential wells in which these minima form are much more isolated from one another in the collinear geometry, and hence more suitable for localizing nuclear wave functions.

These analyzes of the potential energy surfaces showed that for both types of trimers the collinear geometry is preferred. We now turn to the question of which bond lengths are optimal. After finding minima in the complete potential surface, we bin them as a function of R_1 and energy and show them alongside the dimer potential curves in figure 6. The even trimer minima are clustered around and typically just slightly deeper in energy than the dimer minima, but a sizable number of trimer minima are found as far as 20 GHz deeper in energy. From this one can conclude that, although there are exceptions, many trimer minima are found when one bond length is equal to a stable dimer bond length. In the following
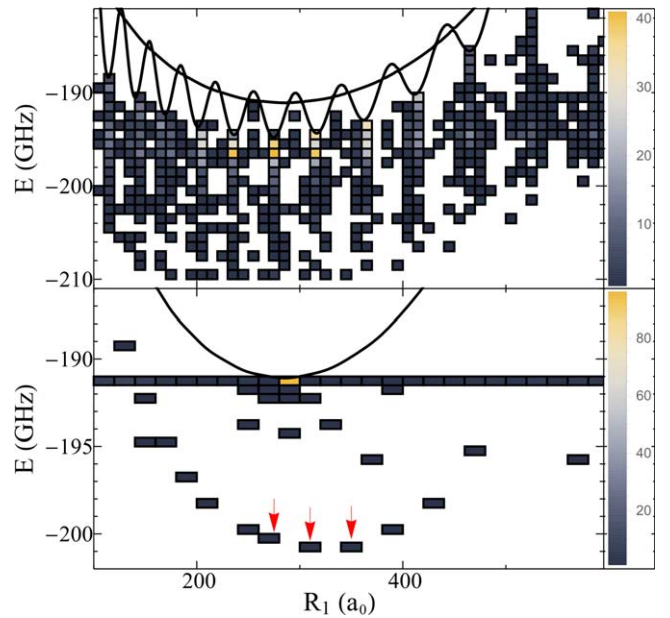

Figure 6. Analysis of the energies and positions of trimer minima. Top: even-trimer; bottom: odd-trimer. The color code indicates the number of minima per bin at energy E and position R_1. The dimer potential energy curves are shown in black. States considered in section 5 are highlighted with red arrows.

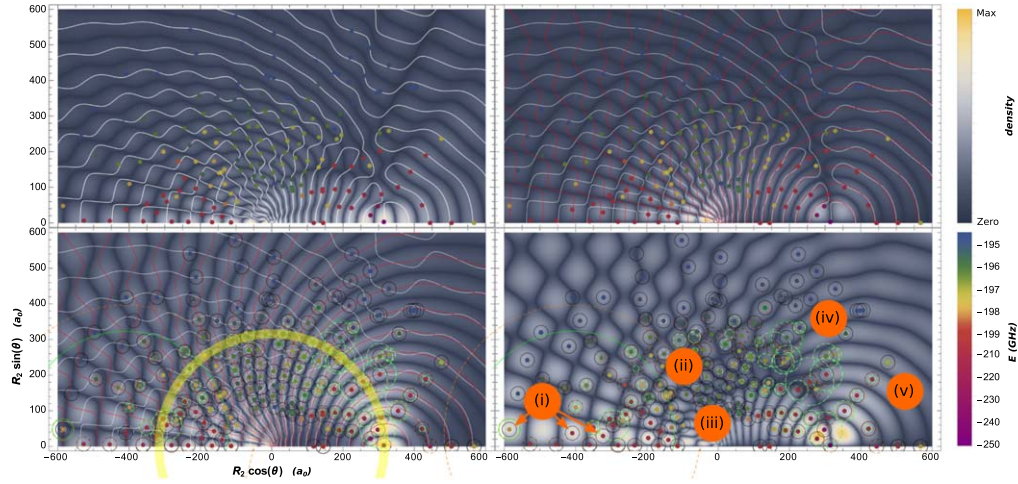J. Phys. B: At. Mol. Opt. Phys. **53** (2020) 084001

M T Eiles *et al*

Figure 7. A study of the even-trimer with one bond length fixed at $R_1 = 316$ a_0. The background density plot in each panel is different, corresponding to $|\Upsilon_{12}^{22}|$ in the top left, $|\Upsilon_{12}^{23}|$ in the top right; $|\Upsilon_{12}^{33}|$ in the bottom left, and $|\Upsilon_{12}^{32}|$ in the bottom right. Positions of the potential energy minima are shown as colored dots in all four panels. The contour lines plotted correspond to $\Upsilon_{12}^{31} = 0$ (red) and $\Upsilon_{12}^{21} = 0$ (white), and are not shown in some panels for clarity. The yellow circle in the bottom left panel indicates $R_2 = R_1$. The other circles in the bottom panels provide information about the electronic state: their radii indicate the amplitude of each dimer orbital, normalized to the R_1-butterfly orbital (black). The R_2-butterfly is orange; the θ_2-butterfly is white, and the θ_1-butterfly is green. Regions of interest expounded upon in the text are labeled in orange in the bottom right panel.

section we will analyze the specific case $R_1 = 316$ a_0 to study the dependence of the minima depths on R_2 and θ, and thus characterize a subset of the stable geometries.

In contrast, the histogram of odd-trimer minima is strongly peaked at the trivial global minimum, $R_0 \approx 286$ a_0, of the dimer potential. At a given $R_1 \neq R_0$ the minimum is most likely found at $R_2 = R_0$ unless the coupling term is very large, which explains the flat band of energies at the dimer minimum, around -191 GHz. At the collinear geometry the coupling becomes large, leading to a few non-trivial deep minima in the semicircle band. The global minimum shifts to $R_1 \approx 316$. We will investigate the vibrational states associated with the marked bond lengths in section 5.

4. Building principles for the even trimer

For the pure trilobite sector of the Rydberg trimer Hamiltonian (equation (4)), it is clear that potential minima are only found at molecular geometries which maximize the matrix element Υ_{12}^{11}. By definition, this implies that the trilobite trimer minima can be found when one perturber sits in a local maximum of the electronic wave function of a stable trilobite dimer. In the butterfly sector (equation (5)) the vectorial nature of the *p*-wave operator complicates this situation. There are now four possible coupling elements to maximize: Υ_{12}^{22} and Υ_{12}^{32}, which correspond to the *derivative* $\frac{\partial}{\partial R}$ of the *R*-butterfly and the θ-butterfly, and Υ_{12}^{33} and Υ_{12}^{23}, the derivative $\frac{\partial}{\partial \theta}$ of the same respective orbitals. One can find minima in the butterfly trimer potential surfaces when the second atom is placed at a point of locally steepest gradient of the wave function of a stable dimer of either the *R*-butterfly or θ-butterfly type.

To study this more complex building principle we show in the four panels of figure 7 density plots of these four derivative terms, respectively. We overlay the potential energy minima (colored dots) associated with $R_1 = 316$ a_0 so that we can correlate the values of R_2 and θ at these minima geometries with features in the wave function gradients. The extremely deep minima (< -210 GHz) are found when $\vec{R}_1 \approx \vec{R}_2$, and we ignore them, as they are expected to be highly modified by the neutral-neutral interatomic interactions that we have neglected. The gradient maxima often coincide with the nodes of either of the two relevant butterfly wave functions, which we depict using white ($\xi = 2$, *R*-butterfly) and red ($\xi = 3$, θ-butterfly) contours.

Consistent with the building principle sketched above, all of the potential minima occur at a nuclear configuration which maximizes at least one gradient. Two concrete examples are the yellow dot at the point (480, 210), which lies at a maximum of all four gradients, and the red dot at (-400, 50), which lies at a maximum of only the two cross-gradients displayed in the right panels. When certain coupling terms dominate at different nuclear configurations, this leads to a rich diversity of possible electronic states described by the linear combination of butterfly orbitals $\Psi(\vec{r}) = \sum_{i=1}^{2}\sum_{\xi=2}^{3} c_i^{(\xi)} \Upsilon_{ir}^{\xi 1}$. In the bottom panels of figure 7 we depict this electronic eigenstate for each minimum configuration using four circles whose radii are proportional to the four mixing coefficients $c_i^{(\xi)}$. The orange circles have radius $|c_2^{(2)}|$, the white circles $|c_2^{(3)}|$, the green circles $|c_1^{(3)}|$; these radii are normalized to the R_1-butterfly amplitude $|c_1^{(2)}|$ (black), which is why some circles (notably in the bottom right panel) can become uncharacteristically large. Along the contour $R_1 = R_2$, highlighted in yellow in the bottom left panel, the electronic state is typically an equal mixture of R_1- and R_2-butterflies which resembles the trilobite trimer studied in previous works [16, 19, 23]. Deep within this circle and far outside of it, the

electronic states tend to be dominated by the R_1-butterfly component. Most of the remaining states are predominantly mixtures of either the two R_1-, R_2-butterflies or the two θ_1-, θ_2-butterflies.

By studying these four panels, one can identify several generic patterns such as these, as well as a few notable exceptions. We have identified five interesting regions of the phase space as labeled in orange:

(i) The states indicated by the arrows at this marker are unique in that they are mixtures of $\xi = 2$ and $\xi = 3$ orbitals. To the immediate left and right of the marker lie states dominated by θ_1- and R_2- butterflies (green and orange, respectively). Further to the right is the opposite case, an equal mixture of R_1- and θ_2- butterflies (black and white, respectively) with vanishing R_2 and θ_1 components. These potential minima are located at the nodes of the Υ_{12}^{22} and Υ_{12}^{33} derivative surfaces (see left panels), but at the maxima of the Υ_{12}^{23} and Υ_{12}^{32} surfaces (right panels); these trimer states are therefore only possible due to the coupling between different types of butterfly states. A trimer of this type can have unusual electronic properties as a result of this coupling, since the $\xi = 2$ and $\xi = 3$ dipole moments have very different magnitudes and even different signs [13, 27].

(ii) Immediately above this marker are two states with nearly equal contributions from all four dimer orbitals; along with a similar state at $(x, y) \approx (-380, 60)$, these seem to be the only states with this composition for $R_1 = 316$ a$_0$.

(iii) Along the $\theta = \pi$ line along the bottom of each panel, the electronic states change from primarily dimer-like at small R_2 to very trimer-like as R_2 increases. By dimer-like we mean that the eigenstate is dominated by the butterfly orbital of a single ground state atom, whereas trimer-like refers to a state which has significant contributions from butterfly states for each orbital, for example an even mixture of R_1- and R_2- butterflies. These potential minima are the deepest found in this geometry and are better isolated from nearby minima than most of the other configurations, allowing for tight localization of vibrational states. In the next section, we find that nearly all of the deep vibrational states found have this type of molecular geometry.

(iv) In this cluster, the states have large θ_1- and θ_2- butterfly mixing (green and white circles), in nearly equal amounts. Further to the left, closer to the (ii) marker, the opposite is mostly true (black and orange circles).

(v) Along this ray, the mixing between all orbitals is high and the minima are deep and well-isolated from other minima out to quite large distances: one of the few vibrational states found at $\theta \neq 0, \pi$ in the following section is positioned in this ray.

Our goal in this phenomenological description of the electronic and nuclear state-space is not to systematically describe or classify all of the trimer states, but simply to reveal some of the rich diversity of possible electronic configurations.

5. Nuclear wave functions and vibrational spectra

Having discussed the electronic structure and the arrangement of minima in the potential energy landscape, we can now present the properties of supported vibrational states. We obtain vibrational wave functions $\chi(R_1, R_2, \theta)$ numerically as eigenstates of the vibrational Hamiltonian

$$
\begin{aligned}
H^{\mathrm{vib}} = & \frac{1}{m}\left[-\frac{\partial^2}{\partial R_1^2} - \frac{\partial^2}{\partial R_2^2} - \cos\theta \frac{\partial}{\partial R_1}\frac{\partial}{\partial R_2} \right] \\
& - \frac{1}{m}\left(\frac{1}{R_1^2} + \frac{1}{R_2^2} - \frac{\cos\theta}{R_1 R_2} \right)\left(\frac{\partial^2}{\partial\theta^2} + \cot\theta\frac{\partial}{\partial\theta} \right) \\
& - \frac{1}{m}\left(\frac{1}{R_1 R_2} - \frac{1}{R_2}\frac{\partial}{\partial R_1} - \frac{1}{R_1}\frac{\partial}{\partial R_2} \right)\left(\cos\theta + \sin\theta\frac{\partial}{\partial\theta} \right) \\
& + \epsilon(R_1, R_2, \theta),
\end{aligned}
\tag{15}
$$

where m is the mass of ^{87}Rb. This Hamiltonian describes the pure vibrational dynamics of the trimer (depending only on R_1, R_2, θ) and can be obtained from the full nuclear Hamiltonian by separating the center-of-mass motion and projecting onto the subspace of conserved relative angular momentum $L = 0$ [20, 23, 33, 34]. The wave functions are normalized as $\int \mathrm{d}R_1 \mathrm{d}R_2 \mathrm{d}\theta \sin\theta |\chi(R_1, R_2, \theta)|^2 = 1$. In our numerical approach we construct the Hamiltonian on a three-dimensional grid in position space using a finite difference representation for the radial degrees of freedom, R_1 and R_2, and a discrete variable representation for the θ direction [35]. According to the spin statistics of ^{87}Rb, we consider only bosonic states with $\chi(R_1, R_2, \theta) = \chi(R_2, R_1, \theta)$.

Fig. 8(a)–(e) presents energies and reduced probability densities of the energetically lowest vibrational states of the odd butterfly. The reduced densities are obtained by averaging the density $|\chi(R_1, R_2, \theta)|^2$ over one or two degrees of freedom, respectively, and contain information about the likelihood to find the trimer in a certain geometry. For instance, we can infer from the radial densities (orange) that the ground-state (a) has a bond length of $R_1 = R_2 = 316$ a$_0$. This state is 30 MHz detuned from the next excited state (b) with a bond length of $R_1 = R_2 = 340$ a$_0$. Both states are spatially well separated and strongly confined to a collinear geometry as indicated by the angular density (blue). The following states (c) and (d) correspond to excitations of asymmetric stretching modes of the states (b) and (a), respectively. The bosonic spin statistics are reflected here by the absence of states with odd numbers of nodes along the asymmetric stretch mode. State (e) populates yet another equilibrium geometry with a bond length of $R_1 = R_2 = 270$ a$_0$. A selection of even higher lying states is shown in figures 8(f)–(j). Some of them exhibit excitations of symmetric stretching modes (f), (h), highly excited asymmetric stretching modes (g), as well as bending modes (i), (j). To an excellent approximation states belonging to the same bond length are well described by an harmonic ladder with spacings of approximately 400 MHz for the asymmetric stretching, 1.2 GHz for the symmetric stretching, and
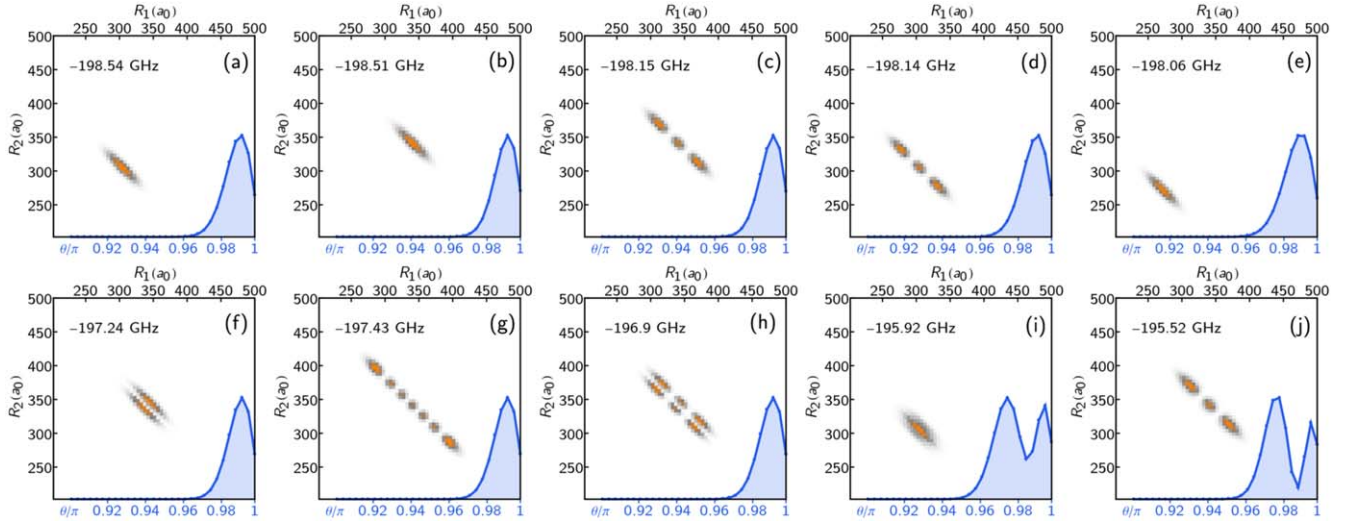
Figure 8. Vibrational states of the odd trimer. Reduced radial probability densities, $\int |\chi(r_1, r_2, \theta)|^2 \sin(\theta) d\theta$, are presented for different states together with their reduced angular densities, $\int |\chi(r_1, r_2, \theta)|^2 \sin(\theta) dr_1 dr_2$, (orange and blue, respectively) and are labeled by their vibrational energies. (a)–(e) are the five energetically lowest states in the specified coordinate range while (f)–(j) are a selection of excited states that illustrate excitations of additional bending and stretching modes. (f) and (h) show symmetric stretch excitations of the configurations of (b) and (c), respectively, while (g) is a highly excited asymmetric stretch state of (b). (i) and (j) have the same stretching excitation as (a) and (c), but an additional bending excitation.
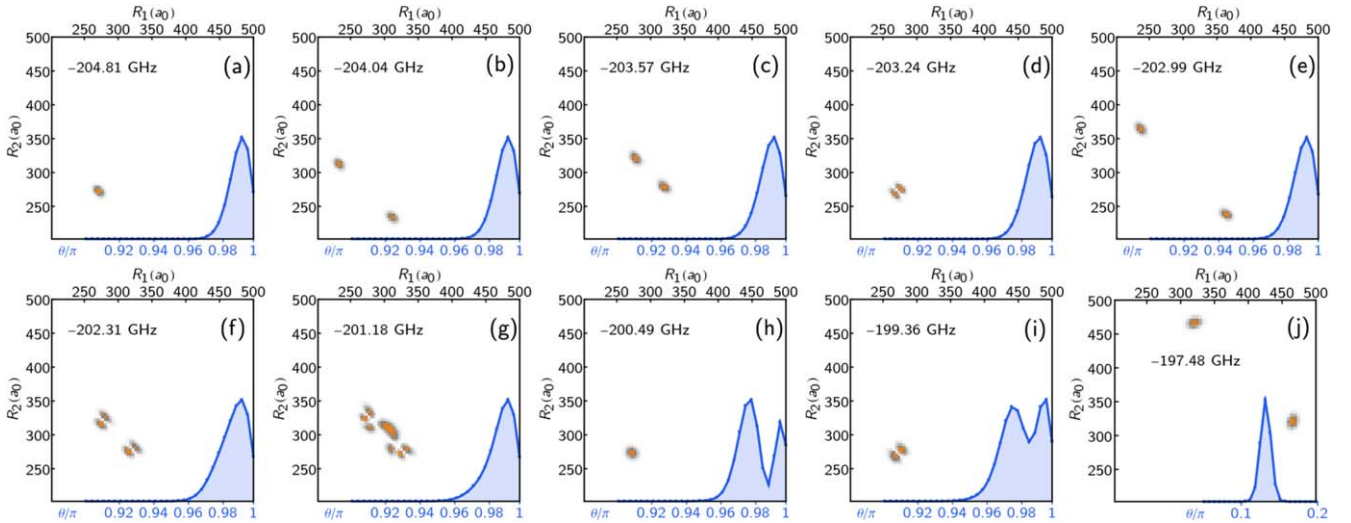

Figure 9. Vibrational states of the even trimer showing similar quantities as in figure 8. (a)–(e) are the five energetically lowest states in the specified coordinate range while (f)–(j) are selected excited states that illustrate effects of delocalization (g) as well as excitations of additional bending (h), (i) and stretching (f), (i) modes, as well as a non-collinear configuration (j).

2.5 GHz for the bending modes. Importantly, the order of these spacings differs from triatomic low-l Rydberg molecules, where the energy spacing of bending motion is typically much smaller than stretching motion [20]. It also differs from the trilobite trimer, as shown by an example in reference [23] where the spacing of bending and stretching modes is almost equal.

Reduced probability densities of the even butterfly trimer are shown in figure 9. Again we present the energetically lowest states (a)–(f) as well as a selection of excited states. Due to the different potential energy surface, the vibrational states of the even trimer differ accordingly in some of their properties from the odd trimer states. First, there are not only symmetric states where both ground-state atoms share the

same bond length (as in panel (a)) but also states where one ground-state atom is always closer to the Rydberg core than the other one, see e.g. (b), (c) and (e). However, due to the bosonic character of the ground-state atoms all densities are symmetric under reflection with respect to the $R_1 = R_2$ diagonal. When these states become excited they can couple to states belonging to different equilibrium configurations to form more complex superpositions, e.g. (g). A second difference is the possibility to form well-localized states in non-collinear arrangements (j). Despite their much more complex underlying electronic structure, vibrational states of the even butterfly trimers are in this respect very similiar to trilobite trimers [23].

J. Phys. B: At. Mol. Opt. Phys. **53** (2020) 084001

M T Eiles *et al*

6. Conclusions

We have extended the analysis of triatomic ultra-long-range Rydberg molecules begun in [20, 23], which focused on low-*l* states and trilobite states, to the butterfly states. These trimers come in two varieties which behave very differently. The odd trimers are only stable in the collinear geometry, have very few equilibrium geometries with equal bond length $R_1 = R_2$, and due to the simple structure of the potential surface at $\theta = \pi$ have nearly independent asymmetric stretch, symmetric stretch, and bending modes. In contrast, the even trimers exhibit complex and vibrant potential surfaces with a rich pattern of potential wells; many of these, however, are insufficiently isolated from other wells to localize vibrational states. As in the odd trimers, many—but not all—of the even trimers have a collinear geometry, but many have equilibrium positions at $R_1 \neq R_2$ and have a more complex excitation spectrum.

Although we have not mentioned in detail the large dipole moments of the dimer orbitals, many of the equilibrium configurations of the even trimer will have non-zero dipole moments stemming from either the asymmetry in bond lengths or the mixing of R- and θ- dimer orbitals. These trimers therefore possess interesting field control possibilities [36]. In the present study we neglected the complex spin structure of these molecules. Including these effects in a polyatomic context is challenging, but will be necessary for quantitative predictions [22]. The mixing of symmetric and asymmetric stretch modes hinted by figure 9(g) implies that the dynamical behavior of vibrational wave packets across these oscillatory potential surfaces will likely be very rich and offer interesting avenues to explore non-adiabatic physics.

Acknowledgments

ORCID iDs

Matthew T Eiles ● https://orcid.org/0000-0002-0569-7551
Peter Schmelcher ● https://orcid.org/0000-0002-2637-0937

References

[1] Andersen T 2004 *Phys. Rep.* **394** 157
[2] Buckman S J and Clark C W 1994 *Rev. Mod. Phys.* **66** 539
[3] Greene C H 1990 *Phys. Rev.* A **42** 1405
[4] Thumm U and Norcross D W 1991 *Phys. Rev. Lett.* **67** 3495
[5] Thumm U and Norcross D W 1992 *Phys. Rev.* A **45** 6349
[6] Scheer M, Thølgersen J, Bilodeau R C, Brodie C A, Haugen H K, Andersen H H, Kristensen P and Andersen T 1998 *Phys. Rev. Lett.* **80** 684
[7] Bahrim C and Thumm U 2000 *Phys. Rev.* A **61** 022722
[8] Bahrim C, Thumm U and Fabrikant I I 2001 *Phys. Rev.* A **63** 042710
[9] Bahrim C, Thumm U, Khuskivadze A A and Fabrikant I I 2002 *Phys. Rev.* A **66** 052712
[10] Eiles M T 2018 *Phys. Rev.* A **98** 042706
[11] Hamilton E L, Greene C H and Sadeghpour H R 2002 *J. Phys. B: At. Mol. Opt. Phys.* **35** L199
[12] Chibisov M I, Khuskivadze A A and Fabrikant I I 2002 *J. Phys. B: At. Mol. Opt. Phys.* **35** L193
[13] Khuskivadze A A, Chibisov M I and Fabrikant I I 2002 *Phys. Rev.* A **66** 042709
[14] Niederprüm T, Thomas O, Eichert T, Lippe C, Pérez-Ríos J, Greene C H and Ott H 2016 *Nat. Commun.* **7** 12820
[15] Eiles M T, Lee H, Pérez-Ríos J and Greene C H 2017 *Phys. Rev.* A **95** 052708
[16] Liu I C H and Rost J M 2006 *Eur. Phys. J.* D **40** 65
[17] Liu I C H, Stanojevic J and Rost J M 2009 *Phys. Rev. Lett.* **102** 173001
[18] Bendkowsky V *et al* 2010 *Phys. Rev. Lett.* **105** 163201
[19] Eiles M, Pérez-Ríos J, Robicheaux F and Greene C H 2016 *J. Phys. B: At. Mol. Opt. Phys.* **49** 114005
[20] Fey C, Kurz M and Schmelcher P 2016 *Phys. Rev.* A **94** 012516
[21] Pérez-Ríos J, Eiles M T and Greene C H 2016 *J. Phys. B: At. Mol. Opt. Phys.* **49** 14LT01
[22] Fey C, Yang J, Rittenhouse S T, Munkes F, Baluktsian M, Schmelcher P, Sadeghpour H R and Shaffer J P 2019 *Phys. Rev. Lett.* **122** 103001
[23] Fey C, Hummel F and Schmelcher P 2019 *Phys. Rev.* A **99** 022506
[24] Fermi E 1934 *Il Nuovo Cimento* **11** 157
[25] Omont A 1977 *J. Phys.* **38** 1343
[26] Anderson D, Miller S A and Raithel G 2014 *Phys. Rev.* A **90** 062518
[27] Eiles M T and Greene C H 2017 *Phys. Rev.* A **95** 042515
[28] Hummel F, Fey C and Schmelcher P 2018 *Phys. Rev.* A **97** 043422
[29] Hummel F, Fey C and Schmelcher P 2019 *Phys. Rev.* A **99** 023401
[30] Eiles M T 2019 *J. Phys. B: At. Mol. Opt. Phys* **52** 113001
[31] Deiß M, Haze S, Wolf J, Wang L, Meinert F, Fey C, Hummel F, Schmelcher P and Hecker Denschlag J 2020 *Physical Review Research* **2** 013047
[32] Tarana M and Čurík R 2016 *Phys. Rev.* A **93** 012515
[33] Carter S and Handy N C 1982 *Mol. Phys.* **47** 1445
[34] Handy N C 1987 *Mol. Phys.* **61** 207
[35] Beck M and Meyer H D 2000 *Phys. Rep.* **324** 1
[36] Kurz M and Schmelcher P 2013 *Phys. Rev.* A **88** 022501